
FOUNDATION MODEL FOR POLYCRYSTALLINE MATERIAL INFORMATICS

Ting-Ju Wei

Department of Civil Engineering
National Taiwan University
Taipei, Taiwan

Chuin-Shan Chen*

Department of Civil Engineering
Department of Materials Science and Engineering
National Taiwan University
Taipei, Taiwan

December 9, 2025

ABSTRACT

We present a 3D polycrystal foundation model that learns a physically structured representation of voxel-based microstructures through large-scale self-supervised pretraining. The encoder is trained on a dataset of 100,000 FCC microstructures whose crystallographic orientations span the texture hull, using a masking strategy that forces the model to infer latent features from incomplete spatial information. The quality of the learned representation is evaluated through two downstream tasks with distinct physical characteristics. (i) Homogenized stiffness prediction: the pretrained encoder consistently outperforms the non-pretrained baseline across all masking ratios. (ii) Nonlinear response modeling: the encoder is coupled with an orientation-aware interaction-based deep material network (ODMN) to infer complete sets of network parameters, enabling accurate stress-strain predictions for previously unseen microstructures. In both tasks, the pretrained encoder demonstrates markedly stronger generalization capability. These results underscore the strong transferability of the proposed framework and its suitability for data-scarce scientific settings, where labeled microstructures are limited and physics-consistent generalization is essential. The foundation model provides a scalable route toward integration with experimentally derived microstructures, offering a new basis for microstructure-property reasoning in practical materials design.

Keywords Foundation model · Polycrystal material · Transfer learning · Self-supervised learning · Masked autoencoder · Deep material network

1 Introduction

Polycrystalline materials constitute the cornerstone of modern engineering applications, as their macroscopic mechanical response is intrinsically governed by the underlying microstructural architecture—most notably the crystallographic texture [1]. Elucidating and quantifying the microstructure-property relationships have therefore become a central pursuit in materials design and performance optimization. The recent surge in artificial intelligence (AI) techniques has further opened up new pathways for establishing data-driven connections between microstructure and properties, thereby accelerating the computational modeling of materials.

In this context, diverse machine learning architectures have been applied to polycrystalline systems. Convolutional neural network (CNN) models such as U-Net have been employed to predict full-field stress distributions in viscoplastic polycrystals [2]. Graph neural networks (GNNs) have proven effective in capturing topological relationships among grains, enabling accurate prediction of effective magnetostriction in heterogeneous polycrystals [3]. Variational autoencoders (VAEs) have been introduced to learn latent representations of electron backscatter diffraction (EBSD) patterns, offering compact and physically meaningful encodings that improve EBSD indexing efficiency [4]. More recently, masked autoencoders (MAEs) have been applied to synthetic 2D polycrystalline datasets for classification

*Corresponding author. Email: dchen@ntu.edu.tw

tasks, which, despite being limited to randomly textured microstructures, have demonstrated the potential of self-supervised learning in texture-informed representation learning [5]. Collectively, these studies highlight the crucial role of latent representation learning, facilitated by machine learning, in advancing microstructure-informed materials modeling.

The concept of a foundation model extends this paradigm by leveraging large-scale pretraining on abundant datasets to learn universal latent representations that are transferable across diverse downstream tasks. Successful precedents include large language models such as BERT and GPT, which derive highly generalizable embeddings from massive text corpora [6, 7]. Analogously, in the materials domain, domain-specific foundation models have begun to emerge. For instance, a masked autoencoder pretrained on synthetic 2D composite microstructures has exhibited remarkable versatility in downstream applications, including nonlinear stress-strain prediction [8].

However, despite the paramount significance of crystallographic textures in governing the anisotropic mechanical response of polycrystalline materials, foundation models explicitly devised for polycrystalline microstructures remain scarcely explored. To address this limitation, we construct a large-scale synthetic dataset by employing hierarchical simplex sampling (HSS) [9, 10] to systematically traverse the complete texture hull of face-centered cubic (FCC) crystals, thereby encompassing the full diversity of the crystallographic texture space. From these sampled texture states, voxel-based polycrystalline microstructures are generated to serve as training data. Building upon this dataset, we develop a 3D voxel-based foundation model for polycrystalline material informatics, which learns texture-aware latent representations through a 3D masked autoencoder architecture. The pretrained model is subsequently fine-tuned for two representative downstream tasks: (1) prediction of homogenized stiffness tensors, and (2) inference of material surrogate model parameters via a linear head applied to the learned latent representations, which are further coupled with crystal plasticity simulations to predict nonlinear microstructural responses.

This study demonstrates the potential of foundation modeling as a unifying framework for polycrystalline material informatics. By pretraining on a large synthetic dataset that systematically spans the crystallographic texture space, the proposed model captures physically meaningful latent representations that generalize across diverse microstructural configurations. These representations not only enable efficient and accurate downstream property prediction but also establish a conceptual bridge between data-driven feature learning and physics-based constitutive modeling. The present work thus lays a scalable pathway toward integrating latent-space learning with multiscale material design and microstructure-informed simulation.

The remainder of this paper is organized as follows. Section 2 details the proposed methodology, including the generation of synthetic datasets, the pretraining of foundation models, and downstream fine-tuning strategies. Section 3 reports and discusses the numerical results obtained for both stiffness prediction and nonlinear response modeling. Finally, Section 4 summarizes the key findings and highlights perspectives for future developments in foundation modeling for polycrystalline materials.

2 Methods

2.1 Overview of the pretrained dataset

The pretraining dataset was designed to comprehensively explore the crystallographic texture space of face-centered cubic (FCC) polycrystals. To achieve this, it is first necessary to define the sampling space of microstructures in terms of their possible crystallographic textures. When a crystallographic texture is represented by the orientation distribution function (ODF), it can be approximated using a discrete basis of Dirac delta functions [11, 12, 13, 9]. In this representation, the ODF takes the form

$$f(q) \approx \sum_{j=1}^J p_j \delta(q, q^{(j)}), \quad (1)$$

where $q \in \text{SO}(3)$ denotes the crystallographic orientation, $\delta(\cdot, \cdot)$ is the Dirac delta function defined on the orientation manifold, $q^{(j)}$ represents a discrete set of fundamental orientations obtained from the discretization of $\text{SO}(3)$, and p_j corresponds to the probability weight associated with each orientation state. The fundamental orientations in this study are uniformly sampled from the fundamental zone of the FCC orientation space, discretized with an angular resolution of 10° , resulting in $J = 618$ fundamental orientations in Eq. (1).

The texture coefficients p_j can be interpreted as probabilistic weights that quantify the likelihood of occurrence for each fundamental orientation. Consequently, the ODF can be expressed in vector form as $\vec{p} = (p_1, p_2, \dots, p_J)$. The convex set spanned by all possible vectors \vec{p} constitutes the so-called texture hull M_H , defined as [9]

$$M_H = \left\{ \vec{p} \mid \vec{p} = (p_1, p_2, \dots, p_J), 0 \leq p_j \leq 1, \sum_{j=1}^J p_j = 1 \right\}. \quad (2)$$

Each point within the texture hull corresponds to a realizable ODF. However, due to the high dimensionality of this convex space, an efficient sampling strategy is required to traverse it. In this study, the HSS algorithm [9, 10] is employed to generate representative ODFs by systematically sampling points \vec{p} within the texture hull. To ensure sufficient coverage of the entire texture domain, a total of 100,000 ODF instances are sampled, each representing a unique crystallographic texture used for constructing the pretraining dataset.

Following ODF generation, each sampled ODF is realized as a representative volume element (RVE) using DREAM.3D-NX [14]. Each RVE consists of a voxel grid of $45 \times 45 \times 45$, containing approximately 810 equiaxed grains. The voxel-wise crystallographic orientations are subsequently reduced to the fundamental zone and converted into quaternion form to ensure rotational continuity and numerical stability for the subsequent self-supervised pre-training stage.

2.2 Self-supervised pretraining stage

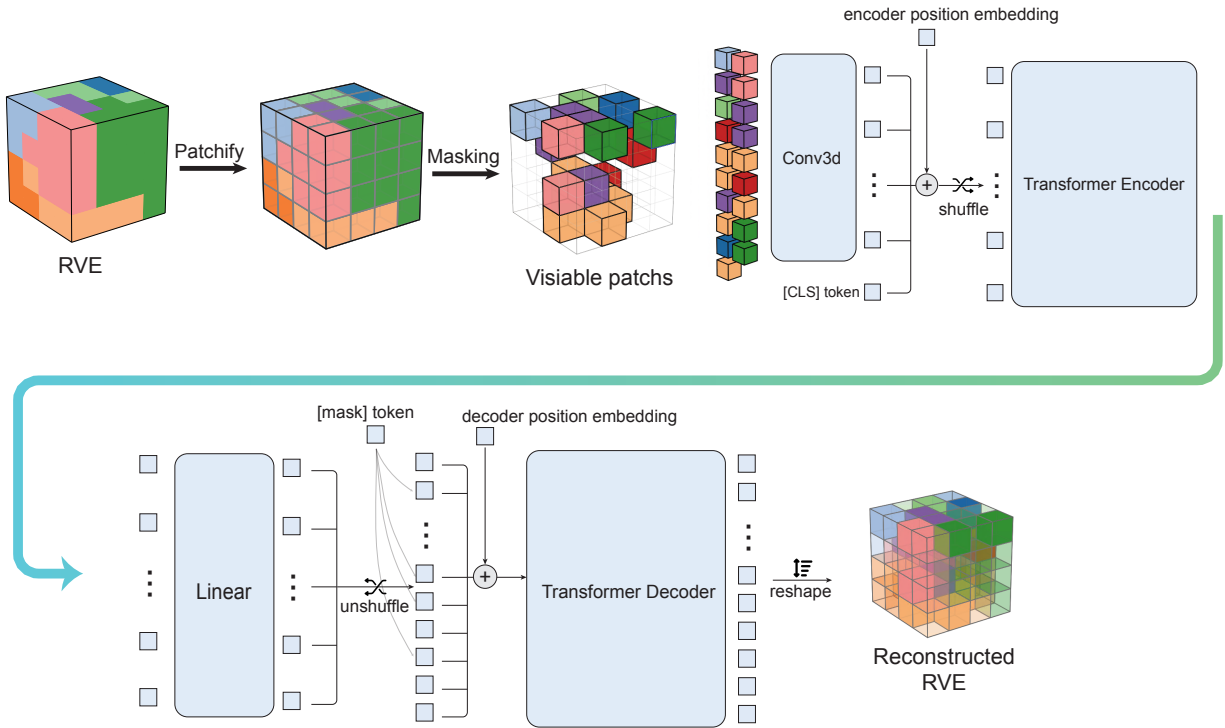


Figure 1: Schematic of the proposed polycrystal foundation model during the pretraining stage. The colored voxel grids within the RVE symbolically indicate different crystallographic orientations and are used for illustrative purposes only.

During pretraining, each voxel-based RVE is represented as a four-dimensional tensor of size $(45, 45, 45, 4)$, where the last dimension corresponds to the quaternion components encoding the local crystallographic orientations within the fundamental zone. The input tensor is partitioned into non-overlapping cubic patches of size $(\mathcal{P}, \mathcal{P}, \mathcal{P}) = (9, 9, 9)$, resulting in $N_p = 125$ patches per training instance. A random subset of these patches is masked according to a prescribed masking ratio (e.g., 40%), leaving 75 visible and 50 masked patches.

Each visible patch is projected into a latent embedding space through a 3D convolutional layer with kernel and stride size $(9, 9, 9)$, generating feature vectors of dimension 768. These embedded tokens are subsequently processed by a transformer-based encoder comprising $\mathcal{N}_e = 12$ blocks, each with an embedding dimension of $\mathcal{D}_e = 768$ and $\mathcal{H}_e = 12$.

self-attention heads. The encoder yields compact latent representations that effectively capture texture-aware features of the polycrystalline microstructure.

A lightweight transformer decoder is subsequently employed to reconstruct the masked patches. The decoder consists of $\mathcal{N}_d = 8$ blocks, each with an embedding dimension of $\mathcal{D}_d = 512$ and $\mathcal{H}_d = 16$ attention heads. Its primary function is to infer the quaternion fields of the missing patches based on the contextual dependencies learned from the visible ones, thereby enforcing spatial and orientational coherence across the reconstructed microstructure.

To encode spatial information, 3D sinusoidal positional encodings (PE) are added to both encoder and decoder inputs following the formulation in [15, 8]. After patchification, the patch grid has dimensions $\mathcal{G} \times \mathcal{G} \times \mathcal{G}$ (with $\mathcal{G} = 5$ in this study). Each coordinate (x, y, z) is independently encoded using sinusoidal functions at multiple frequencies as

$$\begin{aligned} \text{PE}_x^{(2i)}(x) &= \sin\left(\frac{x}{10000^{2i/\mathcal{D}_e}}\right), & \text{PE}_x^{(2i+1)}(x) &= \cos\left(\frac{x}{10000^{2i/\mathcal{D}_e}}\right), \\ \text{PE}_y^{(2i)}(y) &= \sin\left(\frac{y}{10000^{2i/\mathcal{D}_e}}\right), & \text{PE}_y^{(2i+1)}(y) &= \cos\left(\frac{y}{10000^{2i/\mathcal{D}_e}}\right), \\ \text{PE}_z^{(2i)}(z) &= \sin\left(\frac{z}{10000^{2i/\mathcal{D}_e}}\right), & \text{PE}_z^{(2i+1)}(z) &= \cos\left(\frac{z}{10000^{2i/\mathcal{D}_e}}\right), \end{aligned} \quad (3)$$

where $i = 0, 1, \dots, \mathcal{D}_e/2 - 1$.

In addition to positional encoding, a learnable classification token, denoted as [CLS], is prepended to the embedded sequence before it enters the transformer encoder. This token aggregates global microstructural information via the self-attention mechanism. Its positional embedding is set to zero, $\text{PE}_{[\text{CLS}]} = \mathbf{0}$. Thus, the complete positional encoding for the encoder input is

$$\mathbf{PE}_{\text{encoder}} = \text{stack}(\text{PE}_{[\text{CLS}]}, \{\text{concat}(\text{PE}_x(x), \text{PE}_y(y), \text{PE}_z(z)) \mid (x, y, z)\}) \in \mathbb{R}^{(1+N_p) \times \mathcal{D}_e} \quad (4)$$

This asymmetric encoder–decoder architecture mitigates shortcut learning and compels the network to infer high-level statistical dependencies between the visible and missing regions of the microstructure. The pretraining objective aims to minimize the mean squared error (MSE) between the reconstructed quaternion fields $\hat{\mathbf{Q}}_{\text{masked}}^{(i)}$ and their ground-truth counterparts $\mathbf{Q}_{\text{masked}}^{(i)}$ within the masked regions. Each patch has a feature dimensionality of $d = \mathcal{P} \times \mathcal{P} \times \mathcal{P} \times C$, where \mathcal{P} denotes the patch size and C the number of quaternion components. Accordingly, the pretraining loss is formulated as

$$\mathcal{L}_{\text{pretrain}} = \frac{1}{|\mathcal{M}|} \sum_{i \in \mathcal{M}} \frac{1}{d} \left\| \hat{\mathbf{Q}}_{\text{masked}}^{(i)} - \mathbf{Q}_{\text{masked}}^{(i)} \right\|_2^2, \quad (5)$$

where \mathcal{M} represents the set of masked patch indices, and $\|\cdot\|_2$ denotes the Euclidean norm. This objective enforces accurate reconstruction of the masked quaternion fields, thereby guiding the model to learn meaningful spatial–orientational correlations that are essential for downstream microstructural representation tasks.

2.3 Downstream training

After pretraining, the encoder is transferred to downstream stages for task-specific end-to-end fine-tuning. In this phase, the pretrained encoder functions as a microstructure feature extractor, while lightweight task heads are introduced to adapt the learned representations to different predictive objectives. Specifically, the [CLS] token is utilized as the latent feature representation and connected to a linear prediction head to perform two distinct downstream tasks investigated in this study, as introduced below.

2.3.1 Downstream task I: Homogenized stiffness prediction

In polycrystalline materials, the homogenized mechanical response is predominantly governed by the underlying crystallographic texture, which dictates the collective anisotropy emerging from the orientation distribution of constituent grains.

This downstream task aims to evaluate whether the latent representations learned during self-supervised pretraining can be effectively transferred to predict homogenized elastic properties. Specifically, the model is tasked with predicting three principal stiffness components of the homogenized elasticity tensor— \bar{C}_{1111} , \bar{C}_{2222} , and \bar{C}_{3333} —which correspond to the normal elastic moduli along the three orthogonal sample axes. Accurate prediction of these components provides a direct measure of the model’s capability to capture texture-induced anisotropy and to generalize from local orientation features to macroscopic effective responses.

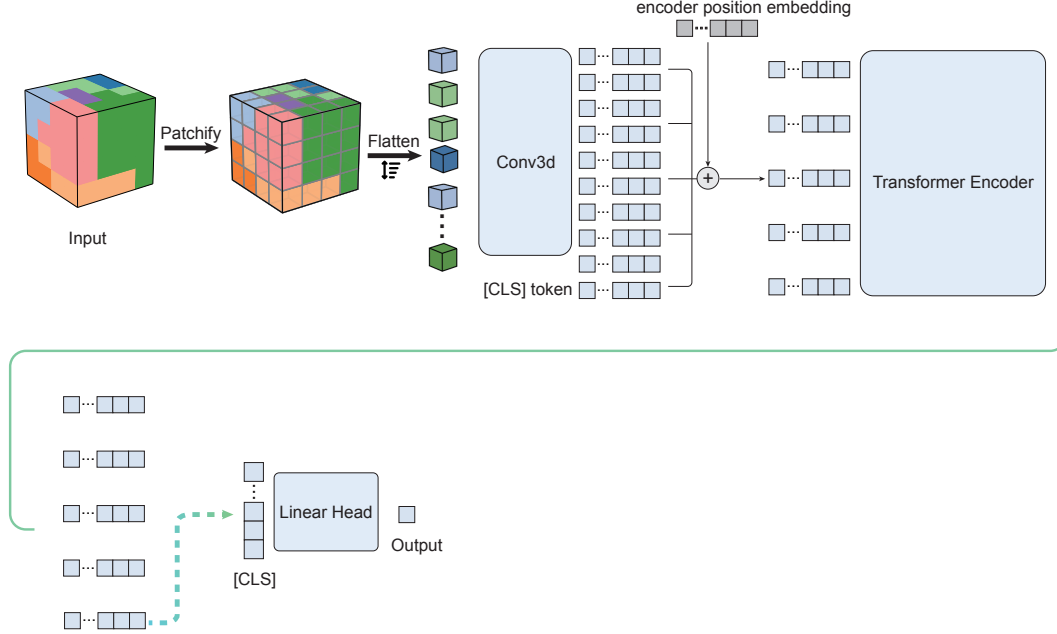


Figure 2: Schematic illustration of the downstream workflow for homogenized stiffness prediction. The pretrained encoder extracts texture-aware latent features, which are subsequently fed into a linear regression head to predict the homogenized stiffness components.

As illustrated in Fig. 2, the pretrained 3D convolutional layer and transformer-based encoder are initialized from the pretraining stage and jointly fine-tuned in an end-to-end fashion. The [CLS] token, which aggregates global information from the entire microstructure through the self-attention mechanism, serves as the latent descriptor of the RVE. A lightweight linear regression head is then appended to this token to map the latent representation to the target stiffness components.

For downstream evaluation, a labeled dataset was constructed to provide ground-truth homogenized stiffness tensors corresponding to a diverse collection of voxel-based RVEs. For each RVE, the ODF was sampled from the convex texture hull using the HSS algorithm, as described in Section 2.1, ensuring statistically representative coverage of the orientation space. Unlike the dataset used for pretraining, which focused solely on learning general orientation correlations in an unsupervised manner, the downstream dataset was specifically designed for supervised regression. A total of 5,000 ODF instances were generated and subsequently realized as voxel-based RVEs using DREAM.3D-NX, each consisting of approximately 810 equiaxed grains discretized on a $45 \times 45 \times 45$ grid. The dataset was randomly divided into 80% for training and 20% for validation to maintain balanced statistical representation across the texture space. The homogenized stiffness tensors of these RVEs were computed using the DAMASK-FFT solver [16] under finite-strain with periodic boundary constraints. Each constituent grain was modeled as a single crystal with cubic elastic symmetry, characterized by the stiffness constants summarized in Table 1.

Table 1: Elastic stiffness constants of the cubic single crystal used in the downstream DAMASK-FFT simulations.

C_{11} (GPa)	C_{12} (GPa)	C_{44} (GPa)
107.3	60.8	28.3

The resulting dataset thus establishes a comprehensive mapping between crystallographic texture and effective elastic response, serving as a benchmark for fine-tuning and quantitatively evaluating the transferability of the pretrained encoder in texture-driven property prediction.

2.3.2 Overview of the deep material networks

In addition to the stiffness prediction task, the second downstream objective extends the pretrained encoder toward modeling nonlinear constitutive responses via predicting the parameters of the orientation-aware interaction-based deep material network (ODMN) [17].

Accurately obtaining the nonlinear mechanical response of RVEs across diverse microstructures is of central importance, particularly in industrial applications where direct full-field simulations are computationally prohibitive. The ODMN framework offers an efficient surrogate modeling strategy for this purpose. It represents a specialized variant of the Deep Material Network (DMN) architecture, designed specifically for polycrystalline materials to account for crystallographic texture effects.

The original DMN [18] formulates a binary-tree-based, physically interpretable architecture that approximates the homogenization mapping between the constituent phase stiffness tensors and the overall homogenized stiffness tensor. Each building block in the binary tree corresponds to a two-phase laminar homogenization unit, in which the volume fraction of the constituent phases and the interface orientation (also referred to as the equilibrium direction) are the only trainable parameters. Since these parameters are directly associated with the geometrical characteristics of the RVE rather than its material constitutive laws, the DMN can be efficiently trained using purely linear elastic data.

A distinctive feature of the DMN framework lies in its ability to perform nonlinear mechanical extrapolation during the online prediction stage, even though the network is trained exclusively on linear elastic stiffness data in the offline phase [18, 19, 20]. This remarkable generalization capability originates from the geometric interpretability of the DMN parameters [21], which encode the microstructural organization instead of the specific constitutive response. During online prediction, the DMN performs a downscaling operation from the macroscopic deformation gradient $\bar{\mathbf{F}}$ to the constituent phases in material nodes, where the local material law is evaluated—potentially exhibiting nonlinear behavior—and then conducts an upscaling process to recover the homogenized first Piola–Kirchhoff stress $\bar{\mathbf{P}}$ and its consistent tangent $\partial\bar{\mathbf{P}}/\partial\bar{\mathbf{F}}$. These upscaling and downscaling operators, constrained by the hierarchical network geometry, enable the DMN and its variants (such as the ODMN) to bridge linear training and nonlinear inference in a physically consistent manner. A detailed mathematical formulation of these operators can be found in previous studies [17, 20].

Despite its interpretability and efficiency, the conventional DMN architecture has an inherent limitation in that its parameters are tied to a specific microstructural realization, which restricts transferability across different RVEs. To overcome this issue, several recent studies have proposed approaches to generalize DMN parameters through interpolation or machine-learning-based frameworks. For example, Huang et al. [22] developed an interpolation scheme to predict DMN parameters for unseen microstructures. In contrast, Jean et al. [23] employed GNNs to infer DMN parameters directly from mesh-based microstructural representations. More recently, Wei et al. [8] demonstrated that foundation models pretrained on large-scale short-fiber composite datasets can act as universal feature extractors for parameter prediction within DMN-like architectures.

Nevertheless, aside from interpolation-based DMN extensions, most of these studies have been limited to two-dimensional composite systems, and their applicability to three-dimensional polycrystalline microstructures remains largely unexplored. Building upon these developments, the present study investigates how a foundation model for polycrystalline microstructures—specifically, the pretrained encoder introduced in Section 2.2—can be fine-tuned to predict ODMN parameters for nonlinear response modeling. This downstream task serves as a rigorous benchmark for assessing both the transferability and the physical fidelity of the learned latent representations in microstructure-sensitive constitutive modeling.

2.3.3 Downstream task II: Nonlinear response modeling

In this work, voxel-based RVEs are used as inputs to the pretrained 3D convolutional and transformer-based encoder. A linear regression head is appended to the [CLS] token to predict the parameters of the ODMN, as illustrated in Fig. 3(a). The ODMN follows a binary-tree topology with a user-defined depth N . The set of trainable parameters for an ODMN of depth N can be expressed as

$$\begin{aligned} \mathcal{F} = & \{z^i, \alpha^i, \beta^i, \gamma^i \mid i = 0, 1, \dots, 2^N - 1\} \\ & \cup \{\theta_p^l, \phi_p^l \mid l = 0, 1, \dots, N - 1; p = 0, 1, \dots, 2^l - 1\} \end{aligned} \quad (6)$$

Here, the ODMN partitions the RVE into 2^N subdomains, each corresponding to a material node within the network hierarchy. The parameters z^i , α^i , β^i , and γ^i represent the volume fraction and local crystallographic orientation of the i -th subdomain, respectively. The angular variables θ and ϕ define the unit normal vector \mathbf{N} that characterizes the equilibrium direction between adjacent subdomains, given by

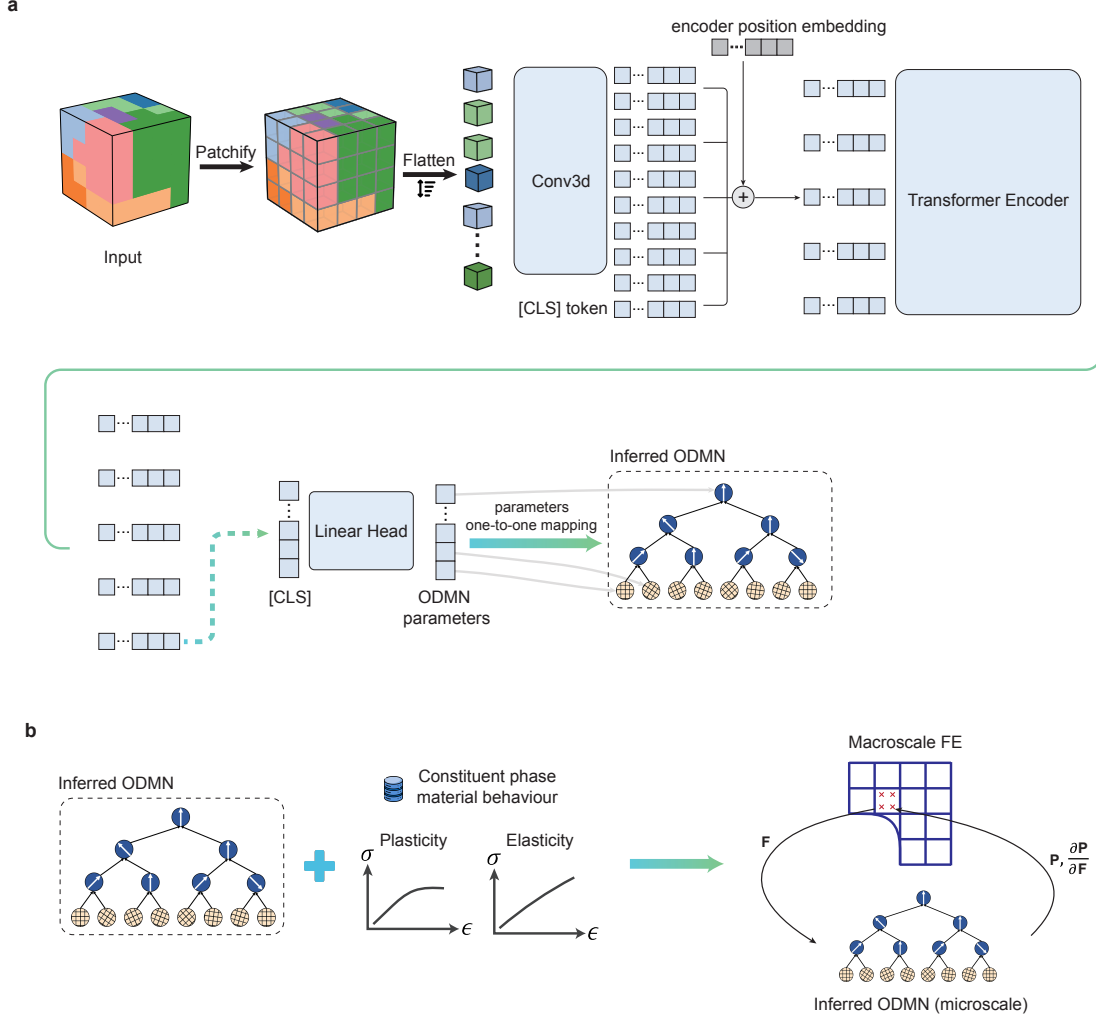


Figure 3: Schematic illustration of the downstream workflow for nonlinear response modeling. (a) During the downstream offline training stage, the pretrained encoder extracts texture-aware latent features, which are subsequently passed through a linear regression head to predict the ODMN parameters. (b) During the online prediction stage, the inferred ODMN is coupled with the constituent phase material behavior to enable nonlinear mechanical response prediction.

$$\vec{\mathbf{N}} = \begin{bmatrix} \cos(2\pi\phi) \sin(\pi\theta) \\ \sin(2\pi\phi) \sin(\pi\theta) \\ \cos(\pi\theta) \end{bmatrix} \quad (7)$$

An ODMN with a binary-tree depth of $N = 6$ is employed as the surrogate model in this work, resulting in a total of $|\mathcal{F}| = 382$ trainable parameters. The end-to-end downstream learning process can be expressed as

$$(\mathbf{Q}) \xrightarrow{\mathcal{M}_{\text{FM}}(\mathbf{Q})} (\mathcal{F}, \mathbf{C}^{\text{crystal}}) \xrightarrow{\mathcal{H}_{\text{ODMN}}(\mathcal{F}, \mathbf{C}^{\text{crystal}})} \bar{\mathbf{C}}, \quad (8)$$

where \mathbf{Q} denotes the quaternion field of the voxel-based microstructure with dimensions $(45, 45, 45, 4)$. The mapping \mathcal{M}_{FM} corresponds to the pretrained encoder equipped with a linear regression head, whose trainable parameters are optimized during fine-tuning to predict the ODMN parameters \mathcal{F} . In contrast, $\mathcal{H}_{\text{ODMN}}$ represents the analytical homogenization function of the ODMN, which deterministically computes the homogenized stiffness tensor $\bar{\mathbf{C}}$ from the predicted \mathcal{F} and the given single-crystal stiffness tensor $\mathbf{C}^{\text{crystal}}$. This downstream coupling enables the pretrained encoder to map texture-informed latent representations to physically interpretable ODMN parameters, thereby unifying data-driven microstructural learning with physics-based constitutive modeling.

During the online prediction stage, unseen microstructures are first processed by the trained mapping \mathcal{M}_{FM} to infer their corresponding ODMN parameters \mathcal{F} . The inferred \mathcal{F} defines a standalone ODMN that can then be coupled with the constituent phase material behavior to predict the nonlinear mechanical response, as illustrated in Fig. 3(b). This approach enables efficient prediction of the nonlinear mechanical behavior of complex polycrystalline microstructures while maintaining the underlying physical consistency of the multiscale framework.

2.3.4 Dataset construction for downstream task II: Nonlinear response modeling

In this downstream task, a labeled dataset was constructed to enable supervised training of the ODMN for nonlinear response modeling. A total of 1,600 distinct voxel-based microstructures were utilized. For each microstructure, 500 different single-crystal stiffness triplets were generated to span a wide range of elastic responses in the training dataset. These 1,600 microstructures were sampled following the approach proposed by Dai et al. [24], in which four representative texture types were designed, each containing 400 samples. The dataset was randomly divided into training and validation subsets, with 320 and 80 samples per texture type, respectively.

For each crystallographic texture, DREAM.3D was employed to generate an RVE consisting of approximately 809 equiaxed grains, discretized into a $45 \times 45 \times 45$ voxel grid. The four representative texture types are summarized as follows:

- (i) Strong-textured-1: One dominant orientation with $Weight = 500,000$ and $Sigma = 1$; all other orientations are assigned $Weight = 1$ and $Sigma = 1$.
- (ii) Strong-textured-2: One dominant orientation with $Weight = 500,000$ and $Sigma = 8$; all other orientations are assigned $Weight = 1$ and $Sigma = 1$.
- (iii) Weak-textured-1: All orientations are uniformly assigned $Weight = 1$ and $Sigma = 1$, corresponding to a nearly random texture.
- (iv) Weak-textured-2: Two dominant orientations, each with $Weight = 500,000$ and $Sigma = 10$; all other orientations are assigned $Weight = 1$ and $Sigma = 1$.

It is worth noting that these texture types represent a subset, rather than a full coverage, of the texture hull; they were intentionally chosen to capture microstructures with distinct texture intensities and orientation dispersions.

After RVE realization, each microstructure was paired with 500 stiffness triplets $\{C_{11}^{\text{crystal}}, C_{12}^{\text{crystal}}, C_{44}^{\text{crystal}}\}$, which together define the single-crystal stiffness tensor $\mathbf{C}^{\text{crystal}}$ used in Eq. (8):

$$\mathbf{C}^{\text{crystal}} = \begin{bmatrix} C_{11}^{\text{crystal}} & C_{12}^{\text{crystal}} & C_{12}^{\text{crystal}} & 0 & 0 & 0 \\ C_{12}^{\text{crystal}} & C_{11}^{\text{crystal}} & C_{12}^{\text{crystal}} & 0 & 0 & 0 \\ C_{12}^{\text{crystal}} & C_{12}^{\text{crystal}} & C_{11}^{\text{crystal}} & 0 & 0 & 0 \\ 0 & 0 & 0 & C_{44}^{\text{crystal}} & 0 & 0 \\ 0 & 0 & 0 & 0 & C_{44}^{\text{crystal}} & 0 \\ 0 & 0 & 0 & 0 & 0 & C_{44}^{\text{crystal}} \end{bmatrix}. \quad (9)$$

The sampling strategy for the triplet set $\{C_{11}^{\text{crystal}}, C_{12}^{\text{crystal}}, C_{44}^{\text{crystal}}\}$ follows the procedure detailed in the original ODMN study [17], ensuring sufficient variability in the elastic anisotropy of the constituent single-crystal phases. The homogenized stiffness tensors $\bar{\mathbf{C}}$ were then computed using the DAMASK-FFT solver [16] under finite-strain conditions with periodic boundary constraints. Each training instance thus consists of $(\mathbf{Q}, \mathbf{C}^{\text{crystal}}, \bar{\mathbf{C}})$, where \mathbf{Q} denotes the quaternion field of the voxel-based microstructure with dimensions $(45, 45, 45, 4)$.

3 Results and Discussion

3.1 Pretraining performance and latent representation analysis

During the pretraining stage, the foundation model is optimized in a self-supervised manner by randomly masking a subset of the voxel-based microstructure and reconstructing the missing regions. The masking ratio therefore serves as a critical hyperparameter, as it directly influences both the difficulty of the reconstruction task and the amount of spatial–orientational information available to the encoder.

To quantify its effect, an ablation study was performed in which the masking ratio was varied from 20% to 90%, with each configuration trained for 1400 epochs. As shown in Fig. 4, all training curves exhibit monotonic decay and stable

convergence, demonstrating that the optimization dynamics remain well behaved across the entire range of masking ratios. The final reconstruction error increases systematically as the masking ratio becomes larger. This behavior is expected: higher masking ratios reduce the number of visible patches, thereby limiting the microstructural information that the model can exploit during reconstruction. The lower reconstruction errors observed at small masking ratios should thus be interpreted as a consequence of increased data availability rather than an indicator of a superior latent representation.

Therefore, reconstruction loss alone does not provide a complete assessment of representation quality. A more rigorous evaluation requires examining how well the learned latent space transfers to downstream tasks, where its ability to encode texture-sensitive microstructural features becomes crucial. Such downstream analyses offer a more meaningful measure of the expressiveness and robustness of the pretrained encoder than reconstruction error obtained during pretraining.

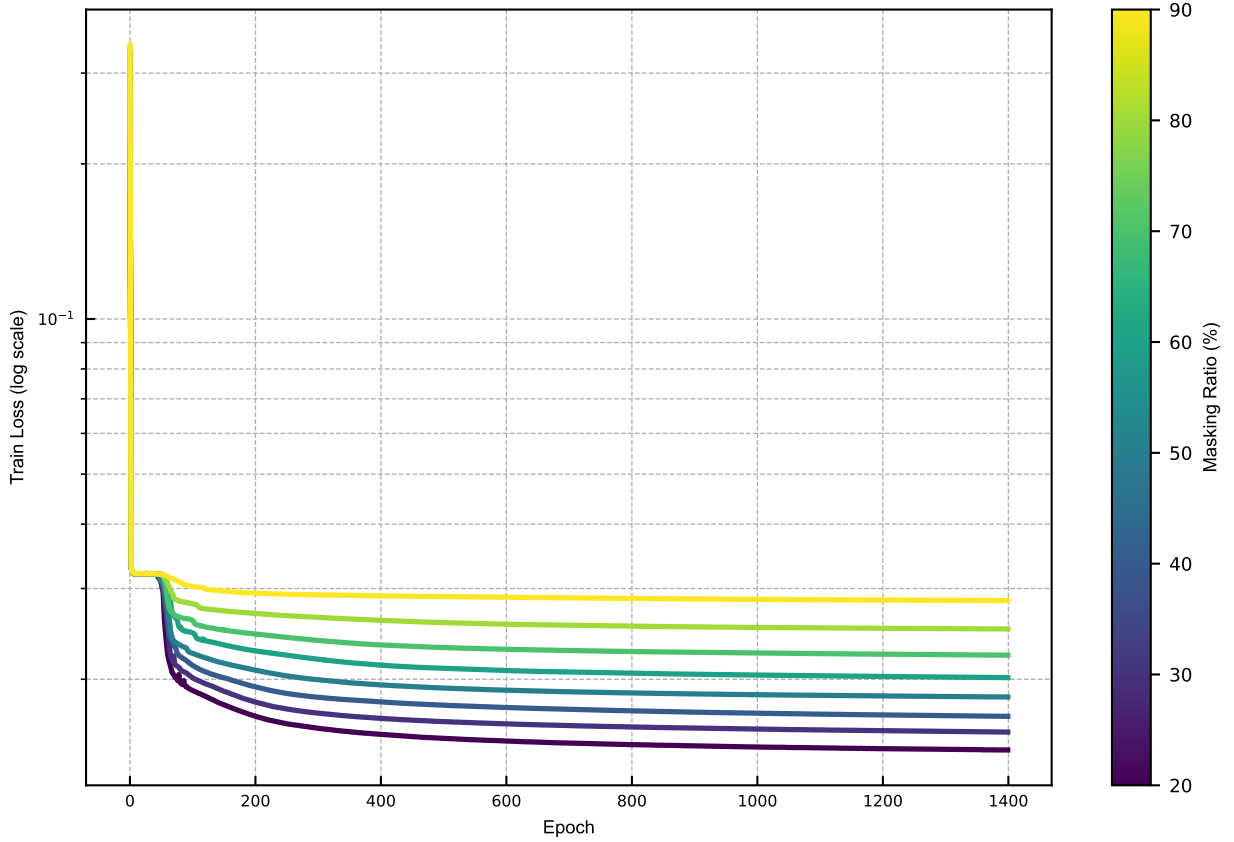


Figure 4: Pretraining loss curves for different masking ratios ranging from 20% to 90%.

Furthermore, the pretraining dataset was generated by sampling the texture hull using the HSS algorithm, which produces broad and diverse coverage of the high-dimensional crystallographic texture distribution space. If the pretrained encoder successfully learns a texture-aware yet unbiased latent representation, the latent distribution of all RVEs in the dataset should exhibit no artificial clustering or preferential structuring.

To evaluate this, the [CLS] token extracted from the pretrained encoder with a masking ratio of 40% at epoch 1400 was used as the latent descriptor for each RVE in the pretraining dataset. These latent vectors were then projected onto a two-dimensional manifold using UMAP for visualization [25]. As shown in Fig. 5, the latent distribution forms an approximately uniform circular topology, indicating that the pretrained encoder produces a smooth and isotropic latent embedding of the entire pretraining dataset. This pattern suggests that the encoder does not collapse the representation into localized regions and is capable of mapping diverse crystallographic textures into a continuous and well-spread latent space, which is desirable for downstream transferability.

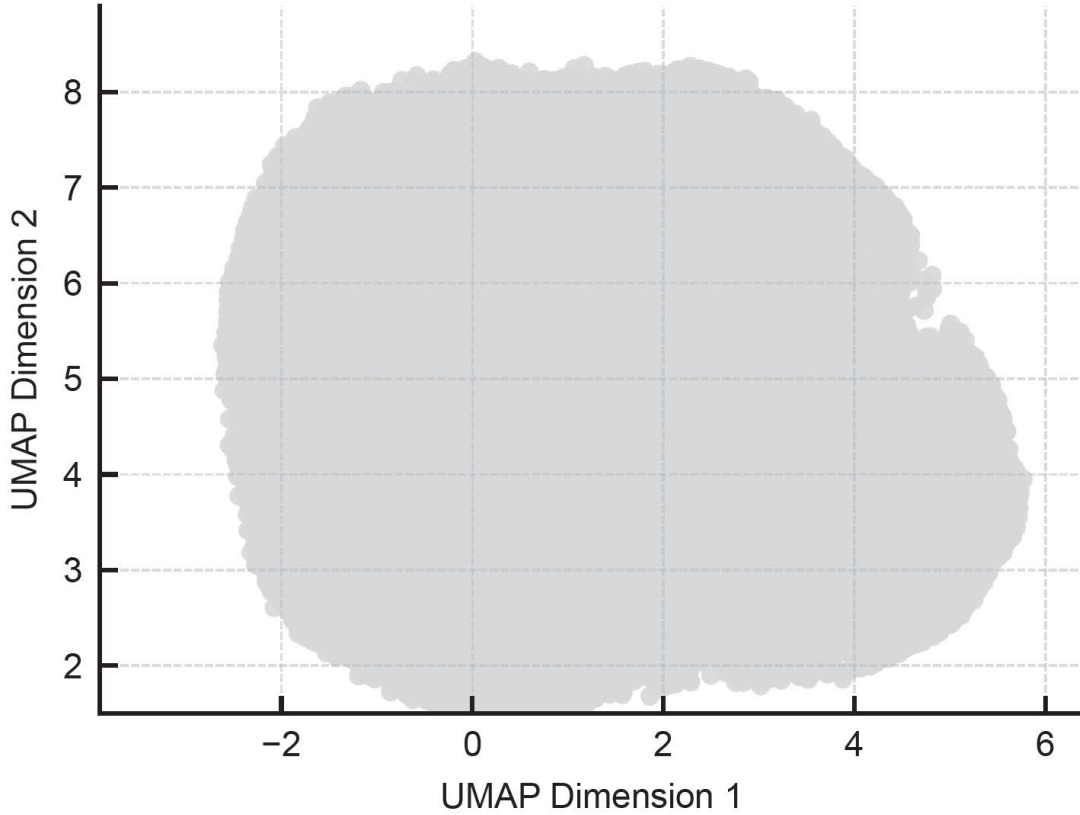


Figure 5: UMAP projection of the latent representations extracted from the pretrained encoder (masking ratio 40%). Each gray point corresponds to a single RVE in the pretraining dataset.

3.2 Downstream task I: stiffness prediction performance

This downstream task evaluates the transferability of the pretrained encoder by predicting the three principal components of the homogenized stiffness tensor, \bar{C}_{1111} , \bar{C}_{2222} , and \bar{C}_{3333} . To assess the benefit of pretraining, models initialized from pretrained encoders with different masking ratios were compared against a baseline model trained from scratch (i.e., without pretraining).

Figure 6 presents the evolution of the training and validation losses for the prediction of the three stiffness components. Across all masking ratios, the models exhibit stable optimization behavior, accompanied by consistent decreases in both losses, indicating that the downstream fine-tuning process follows a stable trajectory of optimization. A clear trend is observed when comparing the pretrained models with the non-pretrained baseline. For every stiffness component and for every masking configuration, the pretrained models achieve markedly lower errors than the model trained

without pretraining. This behavior demonstrates that the latent representation acquired during the self-supervised stage provides a strong inductive structure for predicting texture-dependent elastic properties.

A quantitative summary of the predictive performance is given in Fig. 7, where the validation R^2 values of the three stiffness components are reported. The difference between the pretrained and non-pretrained models is substantial. The model trained from scratch reaches R^2 values below 0.09 for all stiffness components, which is reasonable because the dataset spans the entire texture hull, and the resulting anisotropic responses form a highly complex regression problem when no prior structural information is available.

In contrast, every pretrained configuration yields distinctly higher predictive accuracy even under the data-limited conditions of this downstream task. The model pretrained with a masking ratio of 40% provides the best performance, achieving R^2 values above 0.8 for all three stiffness components. This outcome highlights the importance of self-supervised pretraining. The encoder learns a latent representation that captures essential texture-related features, and this information cannot be obtained effectively when training only on the downstream dataset.

In summary, the results reveal three central findings. First, self-supervised pretraining yields a latent representation that transfers effectively to predicting elastic properties. Second, the masking ratio affects the richness and utility of the learned embedding, resulting in measurable differences in downstream accuracy. Third, the foundation-model pretraining strategy yields a substantial improvement in property regression performance compared to models trained without pretraining.

3.3 Downstream task II: nonlinear response prediction

This downstream task evaluates the transferability of the pretrained encoder by examining its ability to infer ODMN parameters during the offline training stage and its capability to predict nonlinear mechanical responses during the on-line prediction stage. The downstream evaluation, therefore, consists of two major components. The first component focuses on the fine-tuning performance of the pretrained encoder when integrated with the ODMN. The second component assesses the accuracy of the inferred ODMNs when predicting nonlinear stress-strain responses for previously unseen microstructures.

During the offline stage, the pretrained encoder was coupled with the ODMN and optimized in an end-to-end manner to predict the ODMN parameters that approximate the homogenized stiffness responses used for supervised training. The masking ratio used during pretraining was varied from 20% to 90%, and an additional model trained entirely from scratch was included as a baseline.

The training curves presented in Fig. 8 exhibit smooth and stable convergence across all masking configurations. Notably, although the from-scratch model achieves the most minor training error, its validation error is the largest among all configurations. This behavior occurs because, in the absence of pretrained structural priors, the encoder’s representation space is not aligned with the physically meaningful manifold of microstructure features. The latent representations therefore adapt too freely to the supervised samples, driving the training loss down rapidly but resulting in overfitted parameter configurations and poor generalization.

The validation results further highlight the essential role of pretraining. As shown in Fig. 9, the model with a 40% masking ratio achieves the lowest validation error of 2.4%, whereas the model trained without pretraining yields a substantially higher validation error of 10.8%. This contrast illustrates the effectiveness of pretraining in creating a stable representation space that enhances out-of-sample prediction accuracy.

During the online prediction stage, the pretrained model with a 40% masking ratio was selected for evaluation because it achieved the best offline training performance. Four representative RVEs were constructed for testing, corresponding to Strong-textured-1, Strong-textured-2, Weak-textured-1, and Weak-textured-2, denoted as S1, S2, W1, and W2. The trained model processed each microstructure to infer a standalone ODMN, which was subsequently coupled with a crystal plasticity material model to predict the uniaxial loading-unloading stress-strain response [16, 17]. The formulations of the crystal plasticity constitutive model and the elastic response are provided in A and B, respectively, and the material parameters used in the simulations are listed in Table 3. The DNS reference responses were computed using the DAMASK-FFT solver [16].

The resulting stress-strain curves are shown in Fig. 10, where all four microstructures exhibit excellent agreement between the ODMN-predicted and DNS reference responses. To quantitatively assess this agreement, two normalized error metrics were adopted following established definitions in previous studies [8, 22]. The mean relative error measures the average difference between the predicted and DNS stresses, and the maximum relative error captures the most significant deviation over the loading path. These metrics are defined as

$$\text{mean-relative error} = \frac{\frac{1}{n} \sum_{i=1}^n |P_i^{\text{DNS}} - P_i^{\text{ODMN}}|}{\max_{i=1, \dots, n} |P_i^{\text{DNS}}|} \quad (10)$$

$$\text{max-relative error} = \frac{\max_{i=1, \dots, n} |P_i^{\text{DNS}} - P_i^{\text{ODMN}}|}{\max_{i=1, \dots, n} |P_i^{\text{DNS}}|} \quad (11)$$

Table 2: Relative stress prediction errors of inferred ODMNs under cyclic loading, compared against DNS results.

RVE	S1	S2	W1	W2
mean-relative error (%)	1.26	3.93	0.81	0.69
max-relative error (%)	2.07	8.68	3.99	1.87

The quantitative results are summarized in Table 2. Across all four RVEs, the mean relative error remains below four percent, indicating that the inferred ODMNs predict the nonlinear stress response with consistently high accuracy. The most significant maximum relative error occurs in RVE S2, reaching 8.68%. However, this deviation still represents a slight discrepancy relative to the DNS reference and remains well within the tolerance typically considered acceptable for practical nonlinear response prediction.

Overall, these findings demonstrate that integrating the foundation model with the mechanically extrapolative ODMN enables robust prediction of nonlinear responses across previously unseen microstructures with diverse texture characteristics.

Table 3: Elastic and plastic material parameters for AA6022-T4 [26, 27].

N_s	$h_0^{\text{sl-sl}}$ (GPa)	ξ_∞^α (MPa)	ξ^0 (MPa)	n	a	$\dot{\gamma}_0$ (s ⁻¹)	h_{int}^α
12	1.02	266	76	20	3.7	0.001	0

C_{11} (GPa)	C_{12} (GPa)	C_{44} (GPa)	$h^{\text{sl-sl}}$
107.3	60.8	28.3	[1, 1, 5.123, 0.574, 1.123, 1.123, 1]

3.4 Model transferability, interpretability, and current limitations

The capabilities of the proposed foundation model are demonstrated through two downstream tasks with distinct physical characteristics. In Task I, the objective is to predict the homogenized elastic stiffness matrix. Although the target response is linear-elastic, the corresponding input space spans the full crystallographic texture hull, resulting in substantial microstructural variability despite the limited amount of labeled data. In Task II, the evaluation is divided into two stages: the offline training stage and the online prediction stage. During the offline stage, the pretrained encoder is integrated with the ODMN to predict the complete set of ODMN parameters, from which the homogenized stiffness matrix is obtained. In this stage, the model is optimized using labeled homogenized stiffness data to learn the mapping between voxelized microstructures and the corresponding ODMN parameters. Although the training microstructures in Task II cover only a subset of the texture hull, the task is significantly more challenging because it requires learning a high-dimensional and physically structured mapping from microstructural fields to the ODMN’s hierarchical parameterization. During the online prediction stage, the model is evaluated on previously unseen microstructures. The fine-tuned encoder is used to infer a standalone ODMN for each microstructure, and the resulting ODMNs subsequently perform nonlinear extrapolation to carry out crystal-plasticity-based nonlinear homogenization. Thus, Task II simultaneously assesses the transferability of the pretrained encoder and the ability of the ODMN to generalize across microstructures in the nonlinear regime.

To further assess the role of pretraining, a non-pretrained encoder was included as a baseline in both downstream tasks. Across all masking ratios, the non-pretrained encoder consistently delivers noticeably poorer accuracy compared with its pretrained counterpart. An instructive pattern emerges in Task II: the from-scratch model attains a lower training error yet produces a substantially higher validation error than the pretrained model. This discrepancy highlights a fundamental aspect of the fine-tuning process. In the absence of pretraining, the encoder operates within an unconstrained representation space and adapts too closely to the supervised samples, leading to pronounced overfitting and weak generalization. Pretraining, in contrast, organizes the latent space into a physically structured manifold that captures essential microstructural statistics. Although this implicit constraint slows the reduction of training loss, it

provides a valuable inductive bias that guides optimization toward stable and transferable solutions. Such behavior is critical in materials informatics, where labeled data are inherently scarce and generalization to previously unseen microstructures is critical.

Despite these promising results, the present foundation model still exhibits several limitations. The pretraining corpus is restricted to FCC polycrystals with texture variations confined to the crystallographic texture hull, and all grains are assumed to be equiaxed. Future efforts will expand the pretraining dataset to include morphological texture, capturing grain-shape anisotropy, elongated grains, and direction-dependent microstructural patterns. In addition, incorporating experimentally measured microstructures, particularly those produced by additive manufacturing and other process-driven routes, will enable the model to capture real-world heterogeneity more accurately and thereby enhance its robustness and practical relevance.

4 Conclusions

This work introduced a 3D polycrystal foundation model pretrained on a large corpus of FCC microstructures whose crystallographic orientations span the texture hull. Using a self-supervised masking strategy with masking ratios ranging from 20% to 90%, the encoder learned to reconstruct 100,000 voxel-based microstructures and consequently developed a physically meaningful latent space. The resulting latent distribution exhibits an approximately uniform circular topology, indicating that the pretrained encoder produces a smooth and isotropic embedding of the entire pretraining dataset.

The capabilities of the foundation model were demonstrated through two downstream tasks of distinct physical nature. In Task I, the pretrained encoder served as a feature extractor for homogenized stiffness prediction, achieving significantly higher accuracy than the non-pretrained baseline across all masking ratios. In Task II, the encoder was integrated with the ODMN to infer complete sets of ODMN parameters for nonlinear constitutive modeling. The pretrained model not only reduced prediction errors but also yielded stable and transferable ODMN representations for previously unseen microstructures, enabling accurate prediction of nonlinear responses with crystal plasticity.

Collectively, these results demonstrate that the proposed foundation model achieves strong transferability and learns a physically structured latent representation of polycrystalline microstructures. Such properties are particularly valuable in data-scarce scientific settings, where labeled microstructures are expensive to obtain and physics-consistent generalization is essential. The foundation model also has the potential to integrate with experimentally derived datasets. By acting as a latent-space bridge, it allows limited experimental measurements to inform microstructure–property reasoning and strengthen the connection between physical observations and model predictions.

Acknowledgements

This work is supported by the National Science and Technology Council, Taiwan, under Grant 111-2221-E-002-054-MY3, 112-2221-E-007-028, and 114-2221-E-002-010-MY3. We are grateful for the computational resources and support from the NTU-NCREE Joint Artificial Intelligence Research Center and the National Center of High-performance Computing (NCHC). The authors also wish to thank José Niño and Oliver K. Johnson for their valuable assistance with the implementation of the hierarchical simplex sampling and texture hull framework.

A Phenomenological Crystal Plasticity Model

In this study, a phenomenological crystal plasticity model is employed as the local constitutive law in ODMN during online prediction stage. The model follows the formulation implemented in DAMASK and neglects deformation twinning [16]. Plastic deformation is described by the plastic velocity gradient \mathbf{L}_p , which is obtained from the accumulated shear contributions of all slip systems α :

$$\mathbf{L}_p = \sum_{\alpha} \dot{\gamma}^{\alpha} (\mathbf{s}_s^{\alpha} \otimes \mathbf{n}_s^{\alpha}) \quad (12)$$

where \mathbf{s}_s^{α} and \mathbf{n}_s^{α} denote the slip direction and slip-plane normal, respectively, and $\dot{\gamma}^{\alpha}$ is the slip rate of system α .

The slip resistance ξ^{α} evolves according to a hardening law that governs its transition from an initial value ξ_0^{α} toward a saturation level ξ_{∞}^{α} . Its evolution is expressed as

$$\dot{\xi}^\alpha = h_0^{s-s}(1 + h_{\text{int}}^\alpha) \times \sum_{\alpha'}^{N_s} \left| \dot{\gamma}^{\alpha'} \right| \left| 1 - \frac{\xi^{\alpha'}}{\xi_\infty^{\alpha'}} \right|^a \text{sgn} \left(1 - \frac{\xi^{\alpha'}}{\xi_\infty^{\alpha'}} \right) h^{\alpha\alpha'} \quad (13)$$

where N_s is the total number of slip systems and $h^{\alpha\alpha'}$ represents latent hardening interactions.

The slip rate for each system is given by flow rule that depends on the resolved shear stress τ^α and the slip resistance ξ^α :

$$\dot{\gamma}^\alpha = \dot{\gamma}_0^\alpha \left| \frac{\tau^\alpha}{\xi^\alpha} \right|^n \text{sgn}(\tau^\alpha) \quad (14)$$

The resolved shear stress τ^α is calculated using Schmid's law and the Mandel stress \mathbf{M}^P :

$$\tau^\alpha = \mathbf{M}^P \cdot (\mathbf{s}^\alpha \otimes \mathbf{n}^\alpha) \quad (15)$$

B Generalized Hooke's law

In this study, the elastic response within the crystal plasticity used in the ODMN formulation is described by the generalized form of Hooke's law. This constitutive relation links the second Piola–Kirchhoff stress tensor \mathbf{S} to the Green–Lagrange strain tensor \mathbf{E} through the fourth-order elasticity tensor \mathbb{C} :

$$\mathbf{S} = \mathbb{C} : \mathbf{E}. \quad (16)$$

Here, \mathbf{S} denotes the second Piola–Kirchhoff stress, \mathbb{C} is the fourth-order elasticity tensor characterizing the material's elastic moduli, and \mathbf{E} is the Green–Lagrange strain tensor. The symbol $:$ denotes the double contraction between two tensors.

The Green–Lagrange strain is expressed in terms of the elastic deformation gradient \mathbf{F}^e as

$$\mathbf{E} = \frac{1}{2} \left((\mathbf{F}^e)^T \mathbf{F}^e - \mathbb{I} \right), \quad (17)$$

where \mathbf{F}^e represents the elastic part of the deformation gradient and \mathbb{I} is the second-order identity tensor.

Declarations

The authors declare that there are no competing interests.

Author Contributions

Conceptualization and Project Administration: All authors. Investigation and methodology: Ting Ju Wei. Writing—Original Draft: Ting Ju Wei. Review & Editing: All authors. Resources and Funding Acquisition: Chuin-Shan Chen. These author contributions are defined according to the CRediT contributor roles taxonomy.

References

- [1] S Amir H Motaman, Franz Roters, and Christian Haase. Anisotropic polycrystal plasticity due to microstructural heterogeneity: A multi-scale experimental and numerical study on additively manufactured metallic materials. *Acta Materialia*, 185:340–369, 2020.
- [2] Mohammad S Khorrami, Jaber R Mianroodi, Nima H Siboni, Pawan Goyal, Bob Svendsen, Peter Benner, and Dierk Raabe. An artificial neural network for surrogate modeling of stress fields in viscoplastic polycrystalline materials. *npj Computational Materials*, 9(1):37, 2023.
- [3] Minyi Dai, Mehmet F Demirel, Yingyu Liang, and Jia-Mian Hu. Graph neural networks for an accurate and interpretable prediction of the properties of polycrystalline materials. *npj Computational Materials*, 7(1):103, 2021.

- [4] Yu-Chun Liu, Chang-Kai Yeh, Shao-Pu Tsai, and Po-Yen Tung. Learning crystallographic orientations from electron backscatter diffraction patterns using variational autoencoder. *Cell Reports Physical Science*, 6(10), 2025.
- [5] Pierre Belamri, Henry Proudhon, Damien Texier, and David Ryckelynck. Quaternion-based vision-transformer for polycrystalline ebsd scans pre-trained on large-scale synthetic data. *Materials & Design*, page 114599, 2025.
- [6] Jacob Devlin, Ming-Wei Chang, Kenton Lee, and Kristina Toutanova. BERT: Pre-training of deep bidirectional transformers for language understanding. In Jill Burstein, Christy Doran, and Thamar Solorio, editors, *Proceedings of the 2019 Conference of the North American Chapter of the Association for Computational Linguistics: Human Language Technologies, Volume 1 (Long and Short Papers)*, pages 4171–4186, Minneapolis, Minnesota, June 2019. Association for Computational Linguistics.
- [7] Alec Radford, Jeffrey Wu, Rewon Child, David Luan, Dario Amodei, Ilya Sutskever, et al. Language models are unsupervised multitask learners. *OpenAI blog*, 1(8):9, 2019.
- [8] Ting-Ju Wei and Chuin-Shan Chen. Foundation model for composite microstructures: Reconstruction, stiffness, and nonlinear behavior prediction. *Materials & Design*, 257:114397, 2025.
- [9] Oliver K Johnson and Christian Kurniawan. An efficient algorithm for generating diverse microstructure sets and delineating properties closures. *Acta materialia*, 147:313–321, 2018.
- [10] José Niño and Oliver K Johnson. Evolution of crystallographic texture and grain boundary network structure during anisotropic grain growth. *Computational Materials Science*, 240:113023, 2024.
- [11] David T Fullwood, Stephen R Niezgoda, Brent L Adams, and Surya R Kalidindi. Microstructure sensitive design for performance optimization. *Progress in Materials Science*, 55(6):477–562, 2010.
- [12] Tony Fast, Marko Knezevic, and Surya R Kalidindi. Application of microstructure sensitive design to structural components produced from hexagonal polycrystalline metals. *Computational Materials Science*, 43(2):374–383, 2008.
- [13] Oliver K Johnson and Christopher A Schuh. Texture mediated grain boundary network design in two dimensions. *Journal of Materials Research*, 31(9):1171–1184, 2016.
- [14] Michael A Groeber and Michael A Jackson. Dream. 3d: a digital representation environment for the analysis of microstructure in 3d. *Integrating materials and manufacturing innovation*, 3(1):56–72, 2014.
- [15] Ashish Vaswani, Noam Shazeer, Niki Parmar, Jakob Uszkoreit, Llion Jones, Aidan N Gomez, Łukasz Kaiser, and Illia Polosukhin. Attention is all you need. *Advances in neural information processing systems*, 30, 2017.
- [16] F. Roters, M. Diehl, P. Shanthraj, P. Eisenlohr, C. Reuber, S.L. Wong, T. Maiti, A. Ebrahimi, T. Hochrainer, H.-O. Fabritius, S. Nikolov, M. Friák, N. Fujita, N. Grilli, K.G.F. Janssens, N. Jia, P.J.J. Kok, D. Ma, F. Meier, E. Werner, M. Stricker, D. Weygand, and D. Raabe. Damask – the düsseldorf advanced material simulation kit for modeling multi-physics crystal plasticity, thermal, and damage phenomena from the single crystal up to the component scale. *Computational Materials Science*, 158:420–478, 2019.
- [17] Ting-Ju Wei, Tung-Huan Su, and Chuin-Shan Chen. Orientation-aware interaction-based deep material network in polycrystalline materials modeling. *Computer Methods in Applied Mechanics and Engineering*, 441:117977, 2025.
- [18] Zeliang Liu, C. T. Wu, and M. Koishi. A deep material network for multiscale topology learning and accelerated nonlinear modeling of heterogeneous materials. *Computer Methods in Applied Mechanics and Engineering*, 345:1138–1168, MAR 1 2019.
- [19] Wen-Ning Wan, Ting-Ju Wei, Tung-Huan Su, and Chuin-Shan Chen. Decoding material networks: exploring performance of deep material network and interaction-based material networks. *Journal of Mechanics*, 40:796–807, 2024.
- [20] Van Dung Nguyen and Ludovic Noels. Micromechanics-based material networks revisited from the interaction viewpoint; robust and efficient implementation for multi-phase composites. *European Journal of Mechanics - A/Solids*, 91:104384, 2022.
- [21] Dongil Shin, Ryan Alberdi, Ricardo A Lebensohn, and Rémi Dingreville. Deep material network via a quilting strategy: visualization for explainability and recursive training for improved accuracy. *npj Computational Materials*, 9(1):128, 2023.
- [22] Tianyu Huang, Zeliang Liu, CT Wu, and Wei Chen. Microstructure-guided deep material network for rapid nonlinear material modeling and uncertainty quantification. *Computer Methods in Applied Mechanics and Engineering*, 398:115197, 2022.

- [23] Jimmy Gaspard Jean, Tung-Huan Su, Szu-Jui Huang, Cheng-Tang Wu, and Chuin-Shan Chen. Graph-enhanced deep material network: multiscale materials modeling with microstructural informatics. *Computational Mechanics*, 75:113–136, 2025.
- [24] Wei Dai, Huamiao Wang, Qiang Guan, Dayong Li, Yinghong Peng, and Carlos N Tomé. Studying the micromechanical behaviors of a polycrystalline metal by artificial neural networks. *Acta Materialia*, 214:117006, 2021.
- [25] Leland McInnes, John Healy, and James Melville. Umap: uniform manifold approximation and projection for dimension reduction. *arxiv. arXiv preprint arXiv:1802.03426*, 10, 2018.
- [26] Timothy J. Barrett and Marko Knezevic. Deep drawing simulations using the finite element method embedding a multi-level crystal plasticity constitutive law: Experimental verification and sensitivity analysis. *Computer Methods in Applied Mechanics and Engineering*, 354:245–270, 2019.
- [27] Max-Planck-Institut für Eisenforschung GmbH. Damask documentation: Phenopowerlaw aa6022-t4, 2024. Accessed: 21st June 2024.

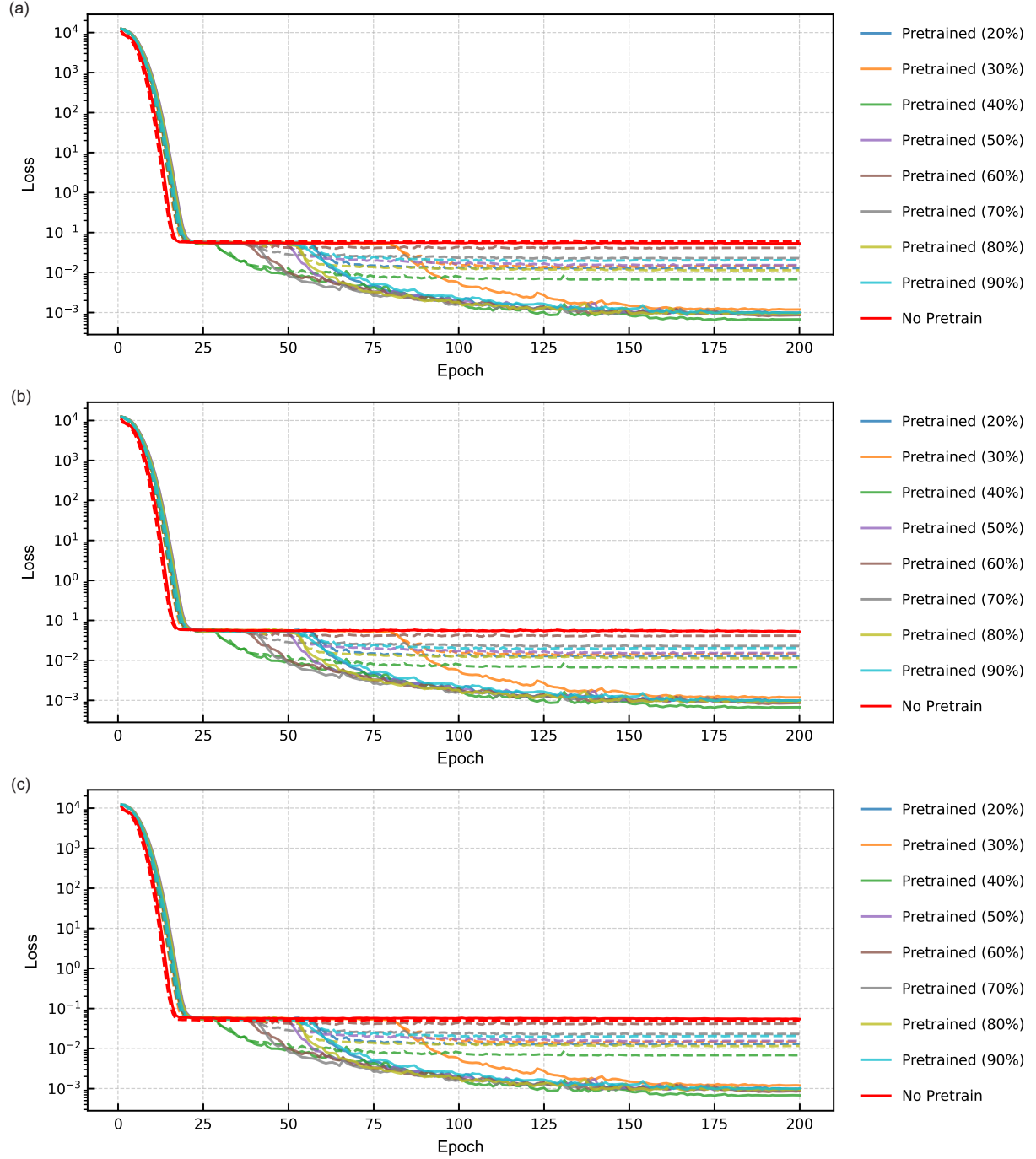


Figure 6: Training and validation loss curves for downstream stiffness prediction of (a) \bar{C}_{1111} , (b) \bar{C}_{2222} , and (c) \bar{C}_{3333} under different masking ratios. Solid lines indicate training loss whereas dashed lines indicate validation loss.

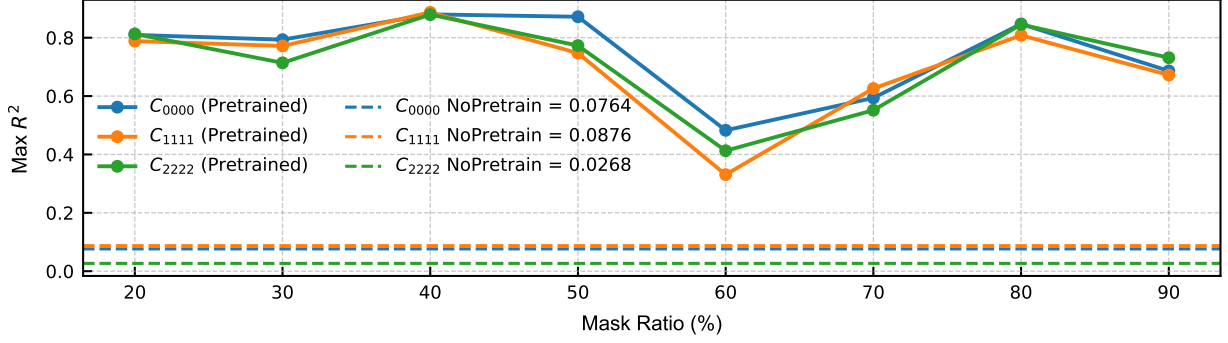


Figure 7: Validation R^2 scores for stiffness prediction of \bar{C}_{1111} , \bar{C}_{2222} , and \bar{C}_{3333} for models trained with and without pretraining.

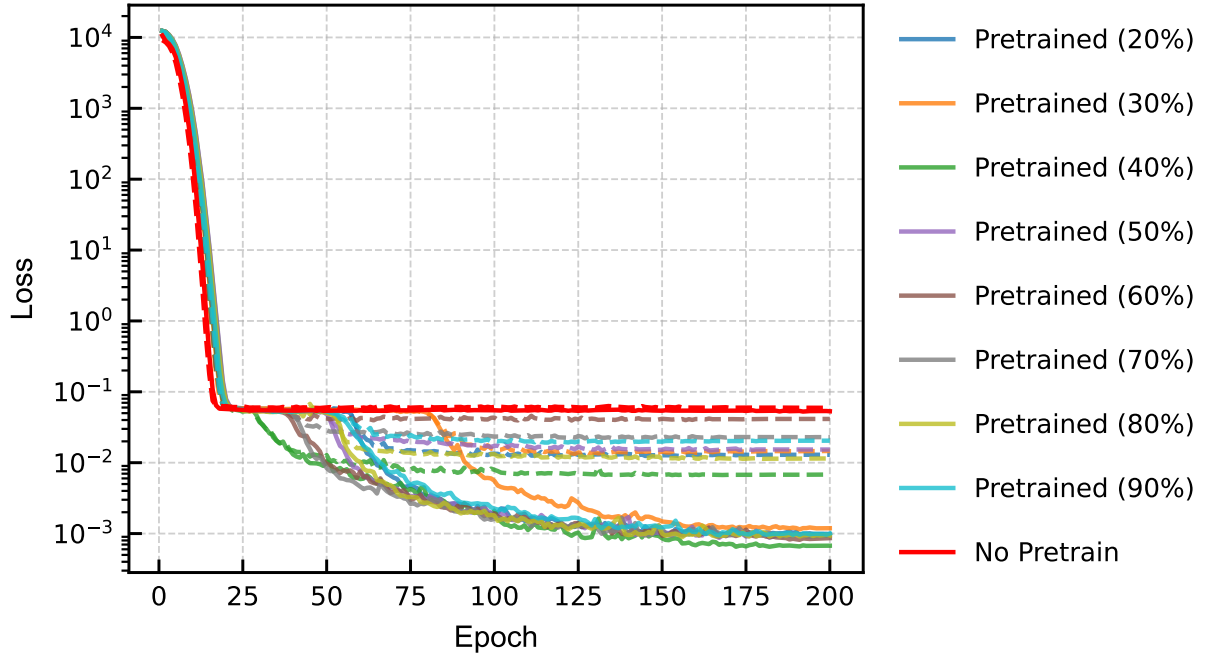


Figure 8: Training and validation loss curves for the downstream task of predicting ODMN parameters under different masking ratios during offline end-to-end fine-tuning. Solid lines denote training loss, whereas dashed lines denote validation loss.

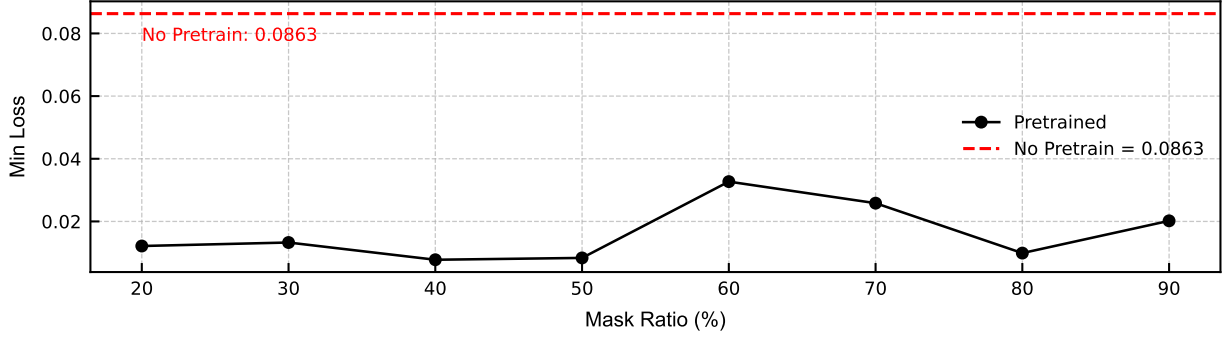


Figure 9: Minimum validation loss for predicting ODMN parameters under different masking ratios during offline end-to-end fine-tuning.

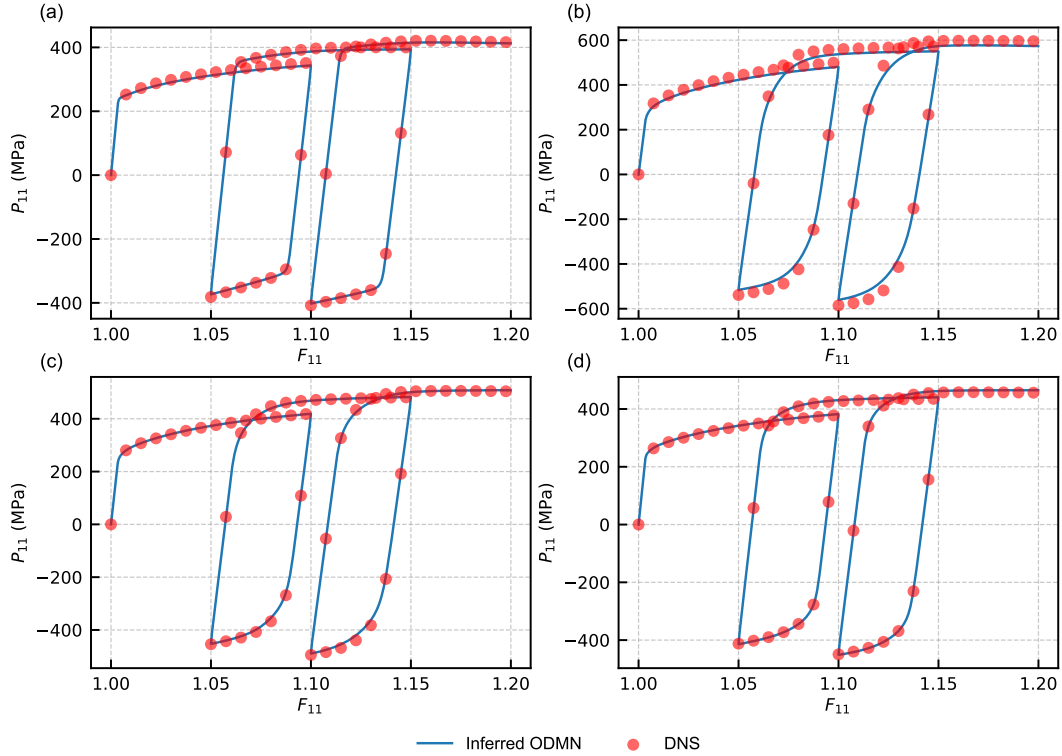


Figure 10: Predicted stress-strain responses obtained from standalone ODMNs inferred for four previously unseen RVEs subjected to cyclic loading. The four cases correspond to (a) S1, (b) S2, (c) W1 and (d) W2.